



**HAL**  
open science

# Absolute cross sections and asymmetry parameters for photodetachment of $C^- - ({}^4S^o)$

Raphaël Marion, Kevin Dunseath, Mariko Terao-Dunseath, Xavier Urbain

► **To cite this version:**

Raphaël Marion, Kevin Dunseath, Mariko Terao-Dunseath, Xavier Urbain. Absolute cross sections and asymmetry parameters for photodetachment of  $C^- - ({}^4S^o)$ . *Physical Review A*, 2021, 103 (2), pp.023115. 10.1103/PhysRevA.103.023115 . hal-03154120

**HAL Id: hal-03154120**

**<https://hal.science/hal-03154120>**

Submitted on 5 Mar 2021

**HAL** is a multi-disciplinary open access archive for the deposit and dissemination of scientific research documents, whether they are published or not. The documents may come from teaching and research institutions in France or abroad, or from public or private research centers.

L'archive ouverte pluridisciplinaire **HAL**, est destinée au dépôt et à la diffusion de documents scientifiques de niveau recherche, publiés ou non, émanant des établissements d'enseignement et de recherche français ou étrangers, des laboratoires publics ou privés.

# Absolute cross sections and asymmetry parameters for photodetachment of $C^-(^4S^o)$

Raphaël Marion,<sup>1</sup> Kevin M. Dunseath,<sup>2</sup> Mariko Terao-Dunseath,<sup>2</sup> and Xavier Urbain<sup>1,\*</sup>

<sup>1</sup>*Institute of Condensed Matter and Nanosciences,  
Université Catholique de Louvain, Louvain-la-Neuve B-1348, Belgium*

<sup>2</sup>*Univ Rennes, CNRS, IPR (Institut de Physique de Rennes) - UMR 6251, F-35000 Rennes, France*

Absolute total cross sections and asymmetry parameters for the photodetachment of the  $^4S^o$  ground state of  $C^-$  are reported for photon energies ranging from threshold to 6 eV. The total cross sections were measured using the Animated Crossed Beam technique incorporating corrections for saturation, while the asymmetry parameters were obtained using Velocity Map Imaging spectrometry. The measured values are in good agreement with theoretical results obtained from an  $R$ -matrix calculation using polarized pseudostates.

PACS numbers: 32.80.Gc, 31.10.+z, 33.60+q

## I. INTRODUCTION

The study of the photodetachment of negative ions, especially of open-shell systems such as carbon and oxygen, presents a double interest: they play an important role in astrophysics and atmospheric physics [1], and provide stringent tests for the description of electron correlation. The electron affinity, or energy difference between the ground states of the negative ion and the residual atom, is indeed much smaller than the ionization energy of atoms and cations. While the variational principle applies *independently* for each system, it is much more difficult to guarantee a well-balanced calculation for *both* systems, and hence an accurate value for the electron affinity.

A comprehensive review of the knowledge of the structure and dynamics of atomic anions has been compiled by Andersen [2], who focused in particular on the decade between 1994 and 2004. In the case of  $O^-$ , there was a long-standing discrepancy between experiment and theory, which was only recently resolved by new measurements using the Animated Crossed Beam technique to determine absolute total cross sections [3]. These are about 17% larger than the earlier data, and are in very good agreement with new theoretical results presented in the same publication. Since the most extensive set of experimental near-threshold photodetachment cross sections for  $C^-(^4S^o)$  dates back to 1962 and was normalized using the earlier data for  $O^-$  [4], a direct measurement appears timely.

The carbon anion exists in two bound states: the ground state  $C^-(1s^2 2s^2 2p^3 ^4S^o)$ , which has an affinity of 1.2621226(11) eV with respect to the  $C(1s^2 2s^2 2p^2 ^3P_0)$  ground level [5], and an excited state  $C^-(1s^2 2s^2 2p^3 ^2D^o)$  which is very weakly bound by about 33 meV [6]. In this work, we consider only photodetachment from the  $^4S^o$  ground state. At low energy, this results in the ejection of a  $2p$  bound electron into the  $s$  or  $d$  wave, leaving the residual atom in its ground state:

$$C^-(1s^2 2s^2 2p^3 ^4S^o) + \gamma \rightarrow C(1s^2 2s^2 2p^2 ^3P) + e^-(\ell = 0, 2).$$

Above 4 eV, it becomes possible to leave the residual atom in its first spin-allowed excited state,  $C(1s^2 2s^2 2p^3 ^5S^o)$ , while ejecting a  $p$ -wave photoelectron:

$$C^-(1s^2 2s^2 2p^3 ^4S^o) + \gamma \rightarrow C(1s^2 2s^2 2p^3 ^5S^o) + e^-(\ell = 1).$$

As the photon energy increases, more final excited states of the residual atom become accessible. In work published just after the review by Andersen [2], Zhou *et al.* [7] computed the photodetachment cross section up to 13 eV, including the excitation of the residual atom up to the  $C(1s^2 2s^2 2p^3 ^5P^o)$  state. At yet higher photon energies, core-hole ionization opens up and multiple photodetachment of  $C^-$  takes place, as studied by Gibson *et al.* [8], and more recently, in the comprehensive work on inner-shell photodetachment conducted by Perry-Sassmannshausen *et al.* [9].

The structure of the paper is as follows: the experimental method used to determine the absolute cross sections and the asymmetry parameter  $\beta$  for photodetachment is described in Sec. II; Sec. III explains how carbon wave functions were optimized in view of new *ab initio*  $R$ -matrix calculations; results and comparison with previous data are detailed in Sec. IV. The conclusions and perspectives for future work are presented in Sec. V.

## II. EXPERIMENT

Our experimental method has been presented in detail in previous publications [3, 10, 11]. We will therefore only describe the main features of the different techniques used in the current work, in particular the novel approach used to determine corrections for saturation effects when using pulsed lasers.

### A. Experimental Setup

The experimental setup can operate in two independent modes and is shown schematically in Fig. 1. The atomic beam is produced by a duoplasmatron source filled with  $CO_2$  gas, at a potential of 4 kV. A permanent

\* xavier.urbain@uclouvain.be

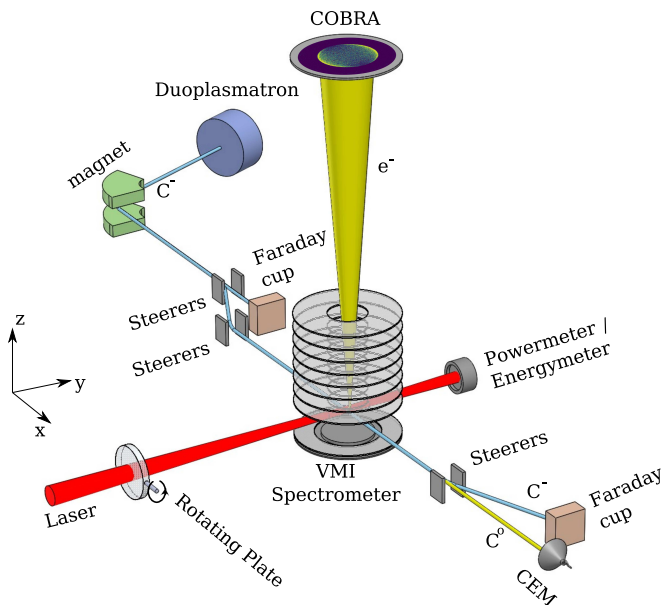


FIG. 1. Experimental setup

78 magnet performs a mass selection and the cleaned and  
 79 collimated beam (diameter 1 mm) is then bunched by an  
 80 electrostatic deflector in front of an aperture to limit de-  
 81 tector ageing. After interaction, residual anions are col-  
 82 lected in a Faraday cup in order to measure the current  
 83  $I_0$ , which is typically 100 pA. Continuous light sources are  
 84 provided by different solid-state lasers at 778 nm, 532 nm  
 85 and 405 nm wavelengths. The pulsed light source is from  
 86 an OPO laser system (NT342A-30 from Ekspla), tunable  
 87 from 2600 nm to 225 nm, with a repetition rate of 30 Hz.  
 88 Photon energies up to 6 eV are reached using an external  
 89 beta barium borate (BBO) crystal.

90 In the first mode, based on the Animated Crossed  
 91 Beam technique, a polarizing beam splitter combined  
 92 with a half-wave plate selects the horizontal polarization  
 93 and tunes the energy of the laser pulses. The animation  
 94 of the laser beam is carried out by rotating a 12 mm  
 95 thick antireflection coated plate whose axis lies perpen-  
 96 dicular to the laser beam propagation axis. The pulse  
 97 energy, tuned to about  $20 \mu\text{J}$ , is measured by a Thorlabs  
 98 ES111C pyroelectric energy sensor while the continuous  
 99 power is measured by a Thorlabs S310C thermal power  
 100 sensor and varied between 40 and 100 mW depending on  
 101 the solid state laser. During experiments with contin-  
 102 uous light, the anion beam current is also continuous while  
 103 with pulsed light, the anions are bunched at 30 Hz in 3.3  
 104 ms packets. In the interaction zone, the anion and pho-  
 105 ton beams cross at right angles. The neutrals follow a  
 106 straight trajectory and are counted with a channel elec-  
 107 tron multiplier (CEM, KBL 25RS from Sjuts Optotech-  
 108 nik) with a high detection efficiency. The anion beam  
 109 is deflected by an electrostatic field and the current is  
 110 measured with a Faraday cup.

111 In the second mode, the VMI spectrometer is turned  
 112 on while working at a higher pulse energy ( $250 \mu\text{J}$ ) with

113 much shorter anion packets ( $1 \mu\text{s}$ ) in order to increase  
 114 the signal-to-noise ratio (SNR). The photoelectrons are  
 115 extracted perpendicularly by an electrostatic plate and  
 116 directed to the electrostatic lens designed following [12].  
 117 The repeller electrode is split to correct the trajectory  
 118 of the anions as explained in [13]. Photoelectrons are  
 119 detected using a COBRA system [14], comprising three  
 120 stacked microchannel plates (MCP), a phosphor screen, a  
 121 metal-oxide semiconductor (CMOS) camera and a wave-  
 122 form digitizer.

123 Data acquisition as well as fast digital control are  
 124 achieved using a field-programmable gate array (FPGA)  
 125 board while the whole setup is supervised by a LabVIEW  
 126 application.

## B. Absolute cross section measurements

### 1. The ACB technique

127  
 128  
 129 The absolute measurement of the cross section is based  
 130 on the Animated Crossed Beam (ACB) technique [10], in  
 131 which the laser beam is periodically swept through the  
 132 perpendicular anion beam. The laser is characterized by  
 133 its frequency  $\omega$ , pulse duration  $T_p$  and, in a reference  
 134 frame whose origin is fixed at the beam intersection in  
 135 the center of the interaction zone, by the flux density  
 136 of photons  $\phi_p(x, y, z - Z, t)$  in the direction of propaga-  
 137 tion.  $Z$  is the offset of the laser beam as it is swept  
 138 across the anion beam. The normalized photon flux den-  
 139 sity,  $\hat{\phi}(x, y, z, t)$ , is assumed to be constant from pulse to  
 140 pulse while the energy  $E_{p,Z}$  may substantially vary for  
 141 each pulse  $p$  of the  $n_Z$  laser shots (typically 120 for good  
 142 statistics) carried out at each offset  $Z$ :

$$\phi_p(x, y, z - Z, t) = \frac{E_{p,Z}}{\hbar\omega} \hat{\phi}(x, y, z - Z, t).$$

143 The  $\text{C}^-$  anions, produced in a duoplasmatron source  
 144 with a bias potential  $-V_S$ , have a nominal velocity  $v =$   
 145  $\sqrt{2eV_S/M_{\text{C}^-}}$ , where  $M_{\text{C}^-}$  is the mass of  $\text{C}^-$  and  $e$  is  
 146 the elementary charge. At any instant during pulse  $p$ ,  
 147 as the velocity  $v \ll c$ , the laser illuminates an almost  
 148 static distribution of anions  $\rho(x, y, z, t)$ , governed by the  
 149 equation

$$\vec{\nabla} \cdot \vec{j} + \frac{\partial \rho}{\partial t} = -\sigma \phi \rho,$$

150 where  $\vec{j} = \rho \vec{v}$  is the anion current density and  $\sigma$  the pho-  
 151 todetachment cross section. The solution of this equation  
 152 for the pulse starting at  $t = t_{p,Z}$  is formally given by

$$\rho_p(x, y, z, t; Z) = \rho(x, y, z; t_{p,Z}) \times \exp \left\{ -\sigma \int_{-\infty}^x \frac{dx'}{v} \phi_p(x', y, z - Z, t - \frac{x - x'}{v}) \right\}.$$

153 The initial distribution of anions,  $\rho(x, y, z; t_{p,Z})$ , can be  
 154 factorized into a normalized distribution  $\hat{\rho}(x, y, z)$  valid

155 for all pulses and a fluctuating magnitude related to the  
 156 total current  $I_{p,Z} = \iint \epsilon p v d y d z$  delivered by the source  
 157 to the entrance of the interaction zone at the time of the  
 158 laser shot:

$$\rho(x, y, z; t_{p,Z}) = \frac{I_{p,Z}}{ev} \hat{\rho}(x, y, z).$$

159 For a detector of neutrals located at a position  $x_d$  far  
 160 after the interaction zone, with an efficiency  $\eta$  and an  
 161 active surface  $S_d$  larger than the cross-sectional area of  
 162 the anion beam, we can express the count of neutrals for  
 163 a pulse  $p$  as

$$N_{p,Z} = \eta \int dt \iint_{S_d} d y d z v \rho(x_d, y, z; t_{p,Z}) \times \left[ 1 - \exp \left\{ -\sigma \int_{-\infty}^{x_d} \frac{d x'}{v} \phi_p(x', y, z - Z, t - \frac{x_d - x'}{v}) \right\} \right]. \quad (1)$$

164 If the argument of the exponential in Eq. (1) is small  
 165 enough so that a first order expansion is sufficient, the  
 166 neutral count  $N_{p,Z}$  is proportional to the cross section  $\sigma$ .  
 167 After normalizing  $N_{p,Z}$  with respect to the current  $I_{p,Z}$   
 168 and energy  $E_{p,Z}$  and integrating over all laser offsets  $Z$ ,  
 169 the remaining integrals involve only  $\hat{\phi}$  and  $\hat{\rho}$ , which result  
 170 in a constant scale factor whose determination does not  
 171 require any further assumptions about the beam profiles.  
 172 We obtain the ACB expression for the photodetach-  
 173 ment cross section:

$$\sigma_{\text{pulsed}}^{\text{ACB}} = \frac{1}{\eta} \sum_Z \frac{\Delta Z}{n_Z} \sum_{p=1}^{n_Z} \frac{\hbar \omega}{E_{p,Z}} \frac{ev}{I_{p,Z}} N_{p,Z}. \quad (2)$$

174 This highlights the major advantage of the ACB tech-  
 175 nique; the experimental cross section does not depend  
 176 on the geometrical overlap of the beams, which is critical  
 177 and difficult to measure accurately in standard beam-  
 178 beam interaction experiments.

179 For continuous lasers, the integration over pulse dura-  
 180 tion is irrelevant and the production rate  $R_Z$  of neutrals  
 181 is directly measured by the CEM and normalized to the  
 182 power  $P_Z$  of the laser beam at position  $Z$  instead of the  
 183 pulse energy  $E_{p,Z}$ , and to the anion current  $I_Z$ :

$$\sigma_{\text{cont}}^{\text{ACB}} = \frac{1}{\eta} \sum_Z \Delta Z \frac{\hbar \omega}{P_Z} \frac{ev}{I_Z} R_Z. \quad (3)$$

## 184 2. Saturation effects from a pulsed laser

185 The ACB technique has been successfully implemented  
 186 and used to determine absolute cross sections for many  
 187 electron-ion [15–17] and electron-atom [18, 19] interac-  
 188 tions as well as for the photodetachment of  $\text{H}^-$  [20] and  
 189  $\text{O}^-$  [3, 11]. The few necessary assumptions that are satis-  
 190 fied in the case of continuous lasers however do not always  
 191 hold for pulsed lasers: as the peak intensity may become

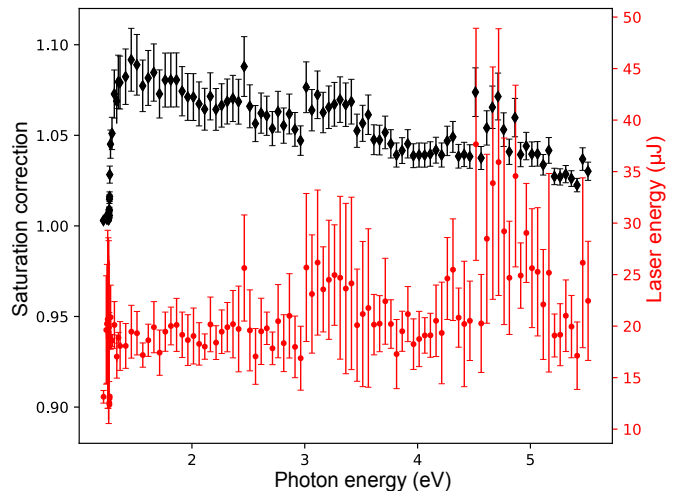


FIG. 2. Correction of saturation for the cross section at each wavelength, and fluctuations of the pulse energy of the laser. Full lozenge: correction of saturation; full circle: pulse energy.

192 high even for pulses of relatively low energy, the first-  
 193 order approximation for the exponential function appear-  
 194 ing in Eq. (1) may be no longer valid, particularly in the  
 195 infrared domain or when the cross section becomes large.  
 196 Higher order terms in the expansion of the exponential  
 197 in Eq. (1) contribute an extra term  $s_p$  representing the  
 198 phenomenon of saturation:

$$\int dt \sum_Z \frac{\hbar \omega}{E_{p,Z}} \left[ 1 - \exp \left\{ -\sigma \int_{-\infty}^{x_d} \frac{d x'}{v} \phi_p \right\} \right] \equiv \frac{\sigma}{v} [1 - s_p(\sigma)].$$

199 Inserting this in Eq. (2) yields a self-consistent expression  
 200 for  $\sigma$  which must be solved by iteration, starting from  
 201  $\sigma_0 = \sigma^{\text{ACB}}$ , until a stationary value of the cross section  
 202 is reached:

$$\sigma_{i+1} = \frac{\sigma^{\text{ACB}}}{1 - s(\sigma_i)}, \quad (4)$$

203 where  $s(\sigma)$  is the correction for saturation averaged over  
 204 the  $n_Z$  laser pulses, taking into account the fluctuations  
 205 of energy shown in Fig. 2.

206 Unfortunately, assumptions concerning the beam pro-  
 207 files are now unavoidable. Provided that the Rayleigh  
 208 length is greater than the diameter of the circular an-  
 209 ion beam, which has a waist  $w_0 \in [250, 300] \mu\text{m}$  and  
 210 a pulse duration  $T_p \in [7, 9] \text{ ns}$ , we can expand the  
 211 laser profile about the coordinates of its maximum  $t_M$   
 212 ( $-T_p/2 \leq t - t_M \leq T_p/2$ ) as

$$\hat{\phi}(x, y, z, t) = \frac{2}{T_p} \frac{2}{\pi w_0^2} \cos^2 \left( \pi \frac{t - t_M}{T_p} \right) \times \exp \left\{ -2 \frac{x^2 + z^2}{w_0^2} \right\}. \quad (5)$$

The factor by which  $\sigma^{ACB}$  must be multiplied to correct for saturation effects is shown in Fig. 2. Its effect is to slightly increase the apparent cross section, particularly at lower photon energies. Since assumptions concerning the beam profiles are needed to estimate the saturation correction, it may seem that the main advantage of the ACB technique is somehow lost. The corrections however remain small and the whole procedure can be validated by comparison with measurements using a continuous laser, which is not subject to saturation, or obtained with a pulsed laser at lower energy and/or higher frequency, as will be shown in Sec. IV.

### C. Differential cross section measurements

In the case of detachment by linearly polarized light, in the dipole approximation, additional information provided by the angular distribution of photoelectrons can be conveniently summarized using the asymmetry parameter  $\beta$ ,

$$\frac{d\sigma}{d\Omega} = \frac{\sigma}{4\pi} [1 + \beta P_2(\cos\theta)], \quad (6)$$

relating the differential cross section  $d\sigma/d\Omega$  to the total cross section  $\sigma$ , where  $P_2$  is the second-order Legendre polynomial and  $\theta$  is the angle between the photoelectron momentum and the laser polarization axis. The parameter  $\beta$  can be measured by means of a Velocity Map Imaging (VMI) spectrometer: photodetachment occurs inside an electric field perpendicular to both the anion beam and the direction of the laser polarization. This electric field slightly bends the trajectory of the anion beam while totally separating out the less energetic photoelectrons. Following [21], this almost perpendicular photoelectron beam is then guided through a thick electrostatic lens formed by stacking biased circular electrodes whose voltages have been optimized by simulation in order to achieve the best resolution. The position sensitive detector is placed at the focal plane where the image formed is the Fourier transform of the transverse momentum of the photoelectron cloud which, in the absence of aberrations, is independent of the location where photodetachment took place.

Outside the lens, the velocity of the photoelectrons depends on the kinetic energy release (KER) of the photodetachment channel and on the bias potential applied to the repeller electrode. The photoelectrons therefore travel on expanding Newton spheres that are projected onto the detector screen. Assuming an azimuthal symmetry, it is possible to reconstruct from the 2D image the 3D angular distribution of the photoelectrons by an inverse Abel transform, for which many computational techniques are available. In this work, we use the MEVELER algorithm based on a Bayesian approach, developed in [22].

## D. Analysis of experimental uncertainties

### 1. Absolute cross sections

By detecting both products of the photodetachment in coincidence, the efficiency  $\eta$  of the CEM can be estimated. Using the logical conjunction symbol  $\wedge$ , we denote by  $(e \wedge l)$  the detection of a photoelectron in coincidence with a laser pulse, and by  $(n \wedge e \wedge l)$  the simultaneous detection of a neutral. Provided all the detected electrons are produced by photodetachment, the binomial statistical estimate of  $\eta$  and its variance are

$$\hat{\eta} = \frac{\#(n \wedge e \wedge l)}{\#(e \wedge l)};$$

$$\text{Var}[\hat{\eta}] = \frac{\hat{\eta}(1 - \hat{\eta})}{\#(e \wedge l)},$$

where the symbol  $\#$  stands for the number of coincidences of a given type. This estimate can be used to calibrate new detectors or to compensate for ageing, with an accuracy of about one percent, depending on the number of events. For the present experiment we have observed a quite stable value of  $\eta = 95 \pm 0.5\%$  during the whole process. To test the method, we have analysed the efficiency of another CEM detector, older and smaller, and obtained a value of  $\eta = 90 \pm 1\%$ .

In ACB measurements with pulsed lasers, two or more events detected during the same laser-neutral coincidence time window will be counted as one. Under normal conditions, with a weak anion current and low photodetachment rates, the probability of such a counting loss is small. We expect the number  $m_p$  of neutrals effectively produced in a pulse to follow Poisson statistics, characterized by a mean value  $\hat{m}$ :

$$P[m_p | \hat{m}] = \frac{\hat{m}^{m_p}}{m_p!} \exp(-\hat{m}),$$

and the number of detected neutrals  $m_d$  to follow binomial statistics :

$$P[m_d = y | \eta, m_p] = \binom{m_p}{y} \eta^y (1 - \eta)^{m_p - y}.$$

The value of  $\hat{m}$  may be deduced from the total number  $m_T$  of counted neutrals for  $n$  pulses by noting that the apparent rate per pulse  $\bar{m} = m_T/n$  ( $\bar{m} < 1$ ) is the complement of the probability of no detection, yielding the relation:

$$\begin{aligned} \bar{m} &= P[m_d \geq 1] = 1 - P[m_d = 0] \\ &= 1 - \sum_{m_p} P[m_d = 0 | \eta, m_p] P[m_p | \hat{m}] \\ &\implies \bar{m} = 1 - e^{-\eta \hat{m}}. \end{aligned}$$

In the following, the quantity  $\eta \hat{m}$  will be denoted by  $\hat{m}_d$ .

298 The background contribution to  $\hat{m}_d$  is estimated by du-  
 299 plicating the coincidence time window with an arbitrary  
 300 delay and applying the same Poisson correction to the  
 301 total number  $b_T$  of neutrals detected out of coincidence  
 302 during the same  $n_Z$  pulses. With these definitions, the  
 303 mean rate and variance for neutral detection per pulse  
 304  $\hat{N}_Z$  entering Eq. (2) is given by

$$\hat{N}_Z = \hat{m}_{d,Z} - \hat{b}_{d,Z};$$

$$\text{Var}[\hat{N}_Z] = \frac{\hat{m}_{d,Z} + \hat{b}_{d,Z}}{n_Z}.$$

305 with  $\hat{m}_{d,Z} = -\ln(1 - \bar{m}_Z)$  and  $\hat{b}_{d,Z} = -\ln(1 - \bar{b}_Z)$ .

306 For continuous light, we have improved the estimate  
 307 of the background compared to our previous setup [3]  
 308 by implementing a mechanical shutter to measure al-  
 309 ternatively the signal and the background  $n_s$  times at  
 310 each offset  $Z$  of the laser beam during the whole sweep  
 311 time, rather than only at the beginning and at the end of  
 312 each experimental run. With a switching delay  $T_s$  lead-  
 313 ing to durations of direct and background measurements  
 314  $T_m = T_b = n_s T_s$ , during which  $m_T$  and  $b_T$  neutrals are  
 315 respectively counted, the detection rate  $\hat{R}_Z$  entering Eq.  
 316 (3) is estimated by

$$\hat{R}_Z = \hat{R}_{m,Z} - \hat{R}_{b,Z};$$

$$\text{Var}[\hat{R}_Z] = \frac{\hat{R}_{m,Z} + \hat{R}_{b,Z}}{n_s T_s},$$

317 with  $\hat{R}_{m,Z} = m_{T,Z}/T_m$  and  $\hat{R}_{b,Z} = b_{T,Z}/T_b$ .

318 The contribution of the variance of the signal to the  
 319 variance of the experimental cross section is given by

$$\text{Var}[\hat{\sigma}_{\text{pulsed}}] = \sum_{p,Z} \left( \frac{1}{n_Z} \frac{\Delta Z}{\eta} \frac{\hbar\omega}{E_{p,Z}} \frac{ev}{I_{p,Z}} \right)^2 \text{Var}[\hat{N}_{p,Z}]$$

$$\text{Var}[\hat{\sigma}_{\text{cont}}] = \sum_Z \left( \frac{\Delta Z}{\eta} \frac{\hbar\omega}{P_Z} \frac{ev}{I_Z} \right)^2 \text{Var}[\hat{R}_Z].$$

320 Sufficient internal statistical precision is usually obtained  
 321 by one  $Z$ -scan for a continuous laser and by 5  $Z$ -scans  
 322 for pulsed light.

323 A final source of uncertainties arises from the ob-  
 324 served fluctuations of measured cross sections over dif-  
 325 ferent runs, which might be due to variations of spatial  
 326 distributions, especially in the laser beam. Fortunately,  
 327 these variations average to zero so that increasing the  
 328 number of runs (a repeatability test) is sufficient to im-  
 329 prove the external statistics and reach the objective of  
 330 2% uncertainty for a pulsed laser and 0.5% for a contin-  
 331 uous laser. The final values are obtained by calculating  
 332 the weighted average over several runs:

TABLE I. Typical values for experimental uncertainties using the ACB technique.

Uncertainties Type A (statistical):	
Detector efficiency	0.5 %
Correction for saturation	1 %
Statistical uncertainties with pulsed laser	2 %
Statistical uncertainties with CW laser	0.5 %
Combined uncertainties type A:	
Pulsed laser	2.3 %
CW laser	0.7 %
Uncertainties Type B (systematic):	
Powermeter / Energymeter	3.1 %
Resolution	0.5 %
Calibration	3 %
Electrometer	1.1 %
Resolution	0.5 %
Calibration	1 %
Vertical displacement Z	2 %
Combined uncertainties type B:	3.8 %
Final combined uncertainties:	
Pulsed Laser	4.5 %
Continuous Laser	3.9 %

$$\hat{\sigma}_{\text{pulsed}}^{ACB} = \sum_j \frac{\hat{\sigma}_j}{\text{Var}[\hat{\sigma}_j]} / \sum_j \frac{1}{\text{Var}[\hat{\sigma}_j]}; \quad (7)$$

$$\text{Var}[\hat{\sigma}_{\text{pulsed}}^{ACB}] = 1 / \sum_j \frac{1}{\text{Var}[\hat{\sigma}_j]}. \quad (8)$$

333 A summary of typical uncertainty values is presented  
 334 in Table I, following [23] for the classifications and rules  
 335 for combining experimental uncertainties.

## 2. Asymmetry parameters

337 To the best of our knowledge, there are no reliable  
 338 statistical estimators for asymmetry parameters. Here  
 339 we propose one such estimator for  $N$  events.

340 We start from a general probability distribution in  
 341 spherical coordinates with azimuthal symmetry:

$$P(v, \theta, \phi) = \frac{p(v)}{4\pi v^2} \left( \sum_{\ell=0}^L \beta_\ell P_\ell(\cos \theta) \right), \quad (9)$$

342 normalized so that

$$\int_0^\infty \int_0^\pi \int_0^{2\pi} dv d\theta d\phi v^2 \sin \theta P(v, \theta, \phi) = 1,$$

343 where  $p(v)$  is the radial velocity distribution normalized  
 344 so that  $\int p(v) dv = 1$  and  $P_\ell$  is the Legendre polynomial  
 345 of degree  $\ell$ . The coefficients  $\beta_\ell$  are then given by

$$\beta_\ell = (2\ell + 1) \int_0^\infty \int_0^\pi \int_0^{2\pi} dv d\theta d\phi v^2 \sin \theta \times P_\ell(\cos \theta) P(v, \theta, \phi). \quad (10)$$

346 The right hand side of this equation can be interpreted as  
 347 the expectation value  $E[X^{[\ell]}]$  of  $X^{[\ell]} = (2\ell + 1)P_\ell(\cos \theta)$   
 348 with respect to the probability distribution  $P(v, \theta, \phi)$ .  
 349 We can also define the variance of  $X^{[\ell]}$  as

$$\begin{aligned} \text{Var}[X^{[\ell]}] &= E[(X^{[\ell]})^2] - \left(E[X^{[\ell]}]\right)^2 \\ &= (2\ell + 1)^2 \sum_{\ell'=0}^L \begin{pmatrix} \ell & \ell & \ell' \\ 0 & 0 & 0 \end{pmatrix}^2 \beta_{\ell'} - \beta_\ell^2. \end{aligned} \quad (11)$$

350 We now consider an experiment providing  $N$  indepen-  
 351 dent observations  $\theta_i$ ,  $i \in \{1, \dots, N\}$ , of the polar angle  
 352  $\theta$ . The sample mean

$$\hat{\beta}_\ell = \frac{1}{N} \sum_{i=1}^N X_i^{[\ell]} = \frac{2\ell + 1}{N} \sum_{i=1}^N P_\ell(\cos \theta_i), \quad (12)$$

353 is then an unbiased estimator which, following the Cen-  
 354 tral Limit Theorem, converges to  $\beta_\ell$  as  $N \rightarrow \infty$ . The ex-  
 355 perimental variance for large sample sizes is  $\text{Var}[X^{[\ell]}]/N$ ,  
 356 which vanishes as  $N \rightarrow \infty$  so that the estimator is consis-  
 357 tent. We note that the presence of the Wigner 3- $j$  symbol  
 358 in Eq. (11) implies that the precision of  $\hat{\beta}_\ell$  is blurred by  
 359 all the even distributions  $P_{\ell'}(\cos \theta)$  with  $\ell'$  even between  
 360 0 and  $2\ell$ .

361 In the specific case of photodetachment by linearly po-  
 362 larized light, the dipole selection rules lead to the expres-  
 363 sion (6) for the differential cross section, which involves  
 364 only  $\ell = 0$  and 2. Since  $\beta_0 = 1$ ,  $\beta_2$  is known as the asym-  
 365 metry parameter commonly denoted  $\beta$ . For the same  
 366 reasons, the upper limit of the summations over  $\ell$  or  $\ell'$   
 367 in Eqs. (9) and (11) is  $L = 2$ . The statistical precision  
 368 for the estimation of  $\beta$ , from Eq. (11) with  $\ell = 2$ , only  
 369 contains contributions from  $\ell' = 0$  and 2, leading to

$$\frac{5}{N} + \frac{10\hat{\beta}}{7N} - \frac{\hat{\beta}^2}{N}. \quad (13)$$

370 These results, however, cannot be directly applied to  
 371 our data since the spherical distribution itself is not  
 372 known experimentally, only its projection. The Abel in-  
 373 version provided by the maximum entropy (MAXENT)  
 374 approach[22] gives an estimate of the distribution in an  
 375 un-normalized form:

$$\mathcal{P}(v, \theta, \phi) = \frac{1}{4\pi v^2} [Q_0(v) + Q_2(v)P_2(\cos \theta)]. \quad (14)$$

376 Integrating Eq. (14) over the velocity space gives the total  
 377 number of events  $N = \int Q_0(v)dv$ , while direct compari-  
 378 son with Eq. (9) yields an estimate  $\hat{\beta}(v) = Q_2(v)/Q_0(v)$ .  
 379 The dependency of  $\hat{\beta}$  on  $v$ , which arises from the unavoid-  
 380 able dispersion associated with the limited precision of  
 381 the experimental setup, prevents a direct determination  
 382 of the best and unique value of the asymmetry parameter  
 383 and its precision from  $Q_0(v)$  and  $Q_2(v)$ , even for cases  
 384 with a single detachment channel.

TABLE II. Typical values for experimental uncertainties in the asymmetry parameters.

Systematic errors:	
Circularization and Abel inversion	$\Delta\beta = 0.01$
Background filtering	$\Delta\beta = 0.01$
Statistical uncertainties:	$\Delta\beta = 0.007$

385 Following Eq. (10), we define the experimental esti-  
 386 mate of  $\hat{\beta}$  as the expectation value of  $X^{[2]}$  with respect  
 387 to the probability distribution (14) normalized by the  
 388 factor  $1/N$ :

$$\begin{aligned} \hat{\beta} &= E[5P_2(\cos \theta)] \\ &= \frac{5}{N} \int_0^\infty \int_0^\pi \int_0^{2\pi} dv d\theta d\phi v^2 \sin \theta \\ &\quad \times P_2(\cos \theta) \mathcal{P}(v, \theta, \phi), \end{aligned}$$

389 which yields

$$\hat{\beta} = \frac{1}{N} \int Q_2(v)dv = \frac{\int Q_2(v)dv}{\int Q_0(v)dv}. \quad (15)$$

390 In practice, the definition of the limits of the integrals  
 391 over  $v$  requires some prior information about the phys-  
 392 ical process in order to define for example the number  
 393 of peaks expected and their energy range. In this work,  
 394 where all the peaks are clearly identified, we select the  
 395 range  $\Delta v$  of  $v$  such that  $Q_0(v)$  is greater than 10% of  
 396 the local maximum. The number of events,  $\int_{\Delta v} Q_0(v)dv$ ,  
 397 is of the order of  $10^5$ , leading to an uncertainty, given  
 398 by Eq. (13), of  $\Delta\hat{\beta} \approx 0.007$ . To these statistical uncer-  
 399 tainties, we add an absolute error  $\Delta\beta = 0.01$  to take  
 400 into account the systematic errors of circularization of  
 401 the data and the internal uncertainties arising from the  
 402 MEVELER algorithm. For photon energies larger than  
 403 3.4 eV, where background noise starts to appear, we in-  
 404 clude an additional  $\Delta\beta = 0.01$  in the absolute error to  
 405 account for filtering in the background procedure. Above  
 406 4 eV, the increasingly large background noise renders the  
 407 filtering procedure less effective and the parameter  $\beta$  be-  
 408 comes inaccessible.

409 Typical values for experimental uncertainties in the  
 410 asymmetry parameters are summarized in Table II.

### III. THEORY

411 Photodetachment cross sections and asymmetry pa-  
 412 rameters were calculated using standard, non-relativistic  
 413  $R$ -matrix theory as implemented in the UK APAP  
 414 (Atomic Processes for Astrophysical Plasmas) suite of  
 415 computer codes [24]. In this approach, initially devel-  
 416 oped in order to study resonances in nucleon-nucleus col-  
 417 lisions [25], configuration space is naturally divided in

two parts: the inner region, where all  $(N + 1)$  electrons interact strongly and the solution is expanded in a basis of discrete functions analogous to bound states in a finite box, built using a set of  $N$ -electron target wave functions coupled to  $R$ -matrix continuum orbitals describing the projectile electron; the outer region, where the solution can be written as the simple product of target and projectile wave functions. In atomic physics, all potentials are known but long-range couplings in the outer region must be fully taken into account. The collisional approach can be extended to photoionization and photodetachment by considering these processes as half-collisions: the asymptotically vanishing initial bound state is the solution of the close-coupling problem with all channels closed. Such a solution only exists for a negative energy that must be found numerically by an iterative approach. In the weak field regime considered here, the photodetachment cross section can be evaluated using perturbation theory: it is proportional to the modulus square of the dipole matrix element between the initial bound state of  $C^-$  and a final continuum state of the neutral atom and an ejected photoelectron. This collisional wave function is determined at each photoelectron energy by matching at the boundary  $a$  the amplitude of the solutions of the inner and outer regions using the inverse log-derivative matrix. Full details of the  $R$ -matrix method are given in [26], in particular chapter 8 which treats photoionization.

In the spectral range covered by our experiment, we consider photodetachment of  $C^-(1s^2 2s^2 2p^3 \ ^4S^o)$ , leaving the residual atom in one of the target states  $C(1s^2 2s^2 2p^2 \ ^3P)$  and  $C(1s^2 2s^2 2p^3 \ ^5S^o)$ . The key point is to determine a set of atomic orbitals suitable, in a configuration interaction approach, for describing electron correlations in the inner region, delimited by the spatial extension of the most diffuse target state. The inner region therefore does not need to encompass the entire charge distribution of  $C^-(1s^2 2s^2 2p^3 \ ^4S^o)$ . The orbitals must of course reproduce as accurately as possible not just the energy levels of the residual atom but also its electron affinity, which is very sensitive to the polarization of the target in the presence of the extra electron. The challenge is to optimize a finite set of orthonormal orbitals while taking into account all these physical effects.

In Table III, we present the parameters of the ten Slater-type orbitals chosen to describe carbon in our  $R$ -matrix calculations. The  $^3P$  and  $^5S^o$  configurations arising from the main configuration  $1s^2 2s^2 2p^2$  with excitation of up to two electrons from the  $n = 2$  shell are included in the basis and the respective hamiltonian matrices are diagonalized. The spectroscopic  $1s$ ,  $2s$  and  $2p$  orbitals are Hartree-Fock orbitals [27]. The other orbitals are optimized using the CIVPOL computer code [28]:  $3s$ ,  $3p$ ,  $3d$  and  $4f$  are optimized on the ground state energy of  $C(^3P)$ ,  $4s$ ,  $4p$  and  $4d$  are optimized on the ground state polarizability.

In Table IV, the energy of  $C(1s^2 2s^2 2p^2 \ ^3P)$  and  $C(1s^2 2s^2 2p^3 \ ^5S^o)$  are compared with the recommended

TABLE III. Parameters of the ten Slater orbitals optimized on the energy and polarizability of the  $C(1s^2 2s^2 2p^2 \ ^3P)$  ground state using the computer code CIVPOL [28].

	$C_{jnl}$	$I_{jnl}$	$\zeta_{jnl}$		$C_{jnl}$	$I_{jnl}$	$\zeta_{jnl}$
1s	23.64032	1	5.43599	2p	0.31061	2	0.98073
	4.04776	1	9.48256		1.58145	2	1.44361
	0.00110	2	1.05749		2.92085	2	2.60051
	-0.00583	2	1.52427		1.27982	2	6.51003
	0.07620	2	2.68435				
	0.15955	2	4.20096	$\bar{3}p$	5.75621	2	1.55007
					-2.37862	3	1.36859
2s	-5.27596	1	5.43599	$\bar{4}p$	2.34572	2	0.51316
	-0.62547	1	9.48256		-3.28476	3	0.68909
	0.10754	2	1.05749		1.03114	4	0.85291
	2.48567	2	1.52427				
	4.57346	2	2.68435				
	-6.16698	2	4.20096	$\bar{3}d$	3.94743	3	1.89468
$\bar{3}s$	6.92570	1	2.34033	$\bar{4}d$	2.78398	3	1.99721
	-20.83502	2	2.37260		-0.17968	4	1.07874
	2.68194	3	1.54022				
$\bar{4}s$	3.86042	1	1.25514	$\bar{4}f$	5.90852	4	2.41065
	-16.39226	2	1.23475				
	17.35377	3	1.61817				
	-0.05982	4	0.91968				

TABLE IV. Energies of the  $1s^2 2s^2 2p^2 \ ^3P$  and  $1s^2 2s^2 2p^3 \ ^5S^o$  terms of carbon, together with those of the three polarized pseudostates included in the  $R$ -matrix calculations. The observed values are taken from the NIST Atomic Spectra Database [29].

	Absolute (a.u.)	Relative (eV)	Zhou <i>et al.</i> [7] (eV)	Observed (eV)
$^3P$	-37.77831	0.0	0.0	0.0
$^5S^o$	-37.62867	4.07191	3.97679	4.17895
$\bar{3}P^o$	-37.40867	10.05842		
$\bar{3}D^o$	-37.31503	12.60649		
$\bar{3}S^o$	-37.26368	14.00380		

values from NIST and those of an earlier calculation by Zhou *et al.* [7], who used a similar  $R$ -matrix approach combined with the Variable Phase Method (VPM) in the asymptotic region. The energy of the  $^5S^o$  level with respect to that of the ground state differs by 2.6% from the observed value and can be considered as sufficiently good for the purpose of this work. The full average polarizability  $\bar{\alpha}$  of  $C(1s^2 2s^2 2p^2 \ ^3P)$  obtained by including  $\bar{3}S^o$ ,  $\bar{3}P^o$  and  $\bar{3}D^o$  pseudostates is  $11.58 a_0^3$ , close to the value of  $11.67 a_0^3$  from an extensive coupled cluster calculation [30].

The electron affinity of the carbon ground state is calculated using the program STGB in the UK APAP suite of codes [24]. This uses a perturbative treatment of the

491 long-range potentials in the  $R$ -matrix outer region combined with an iterative search over negative energies to  
 492 find bound state solutions for the  $(N+1)$ -electron system.  
 493 The value of the electron affinity will thus depend of the  
 494 size of the  $R$ -matrix inner region and the number of con-  
 495 tinuum orbitals used (a larger inner region requires more  
 496 continuum orbitals to ensure convergence). In addition,  
 497 we found that it was necessary to include excitation of  
 498 at least two electrons from the  $1s^2 2s^2 2p^3$  base configu-  
 499 ration in order to obtain a bound state of  $C^-$ . For the  
 500 results reported below, we in fact included excitation of  
 501 up to 3 electrons. For an inner region size varying be-  
 502 tween  $25 a_0$  and  $35 a_0$  and the number of continuum or-  
 503 bitals between 25 and 50, we obtained values of the elec-  
 504 tron affinity ranging from 1.2575 eV to 1.2613 eV, which  
 505 compare favourably with the value of 1.2658 eV corre-  
 506 sponding to the energy difference between the weighted  
 507 average of the experimental fine structure levels of  $C(^3P)$   
 508 and the  $C(^4S^o)$  ground state [5]. The electron affinity  
 509 in the calculation by Zhou *et al.* [7] is 1.21 eV.  
 510

## 511 IV. RESULTS AND DISCUSSION

### 512 A. Total cross sections

513 The absolute cross sections for photodetachment of  
 514  $C(^4S^o)$  from our experiment are presented in Fig. 3 and  
 515 compared with those by Seman and Branscomb [4] and  
 516 Haeffler *et al.* [31]. Other data in the threshold region by  
 517 Feldmann [6], Hall *et al.* [32] and Brandon *et al.* [33] are  
 518 not reproduced here as they are not absolute and cover a  
 519 very limited range of photon energies. Further discussion  
 520 of their work can be found in the review by Andersen [2].

521 We first note that the cross section does not fall to  
 522 zero below the photodetachment threshold of  $C(^4S^o)$ ,  
 523 which indicates that some anions are produced in the  $^2D$   
 524 excited state. Several control measurements from thresh-  
 525 old to a photon energy of 2.7 eV were conducted using  
 526 the VMI spectrometer to determine the branching ra-  
 527 tio between each channel. We found that the branching  
 528 ratio is almost constant at 2% throughout the controlled  
 529 range, except around 1.38 eV, just above threshold, where  
 530 it reaches at most 4%. As this quantity depends on both  
 531 the population and the cross section of each state entering  
 532 the beam composition, the problem is not experimentally  
 533 constrained. We will address this in future work, but  
 534 some insight can be gained from the theoretical study  
 535 by Zhou *et al.* [34], which suggests that the cross section  
 536 for photodetachment of  $C(^2D)$  is of a similar order of  
 537 magnitude to that for photodetachment of  $C(^4S^o)$  over  
 538 the energy range considered, with a small peak above  
 539 the  $^4S^o$  photodetachment threshold. This in turn sug-  
 540 gests that the population of  $C(^2D)$  in our anion beam  
 541 is very small and that the measured cross sections are  
 542 relatively unaffected by the presence of this state. Even  
 543 in the worst case, near threshold, the estimate of the er-  
 544 ror obtained by combining the measured branching ratio

545 and the theoretical cross section is of the order of 1.5%,  
 546 less than the experimental uncertainty.

547 Just above threshold, the cross section increases as  
 548  $\sqrt{E}$ , where  $E$  is the photoelectron energy, since the dom-  
 549 inant channel is  $C(1s^2 2s^2 2p^2 ^3P) + e^-(\ell = 0)$ . Beyond  
 550 1 eV, it increases slightly with photon energy before a  
 551 small dip in the vicinity of the  $C(1s^2 2s 2p^3 ^5S^o)$  thresh-  
 552 old, followed by a steep increase due to the opening of  
 553 the  $C(^5S^o) + e^-(\ell = 1)$  channel.

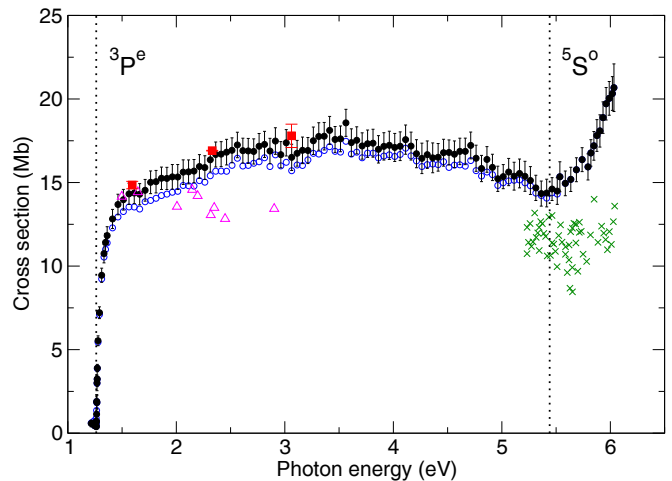


FIG. 3. Experimental cross sections for photodetachment of  $C(^4S^o)$  as a function of the photon energy. Full circle: present work with a pulsed laser and correction for saturation; open circles: present work with a pulsed laser without correction for saturation; full square: present work with a continuous laser. Error bars for the pulsed laser correspond to one standard deviation as estimated by expression (8). Open triangles: Seman and Branscomb [4]; crosses: Haeffler *et al.* [31]. Vertical dotted lines: positions of the  $C(^3P)$  and  $C(^5S^o)$  thresholds.

554 In the wake of their pioneering work on the photode-  
 555 tachment of  $O^-$  [35, 36], Seman and Branscomb [4] inves-  
 556 tigated  $C^-$  in the spectral region between 0.4 and 2.6  $\mu\text{m}$   
 557 (0.478 eV – 3.1 eV). Their relative cross sections were nor-  
 558 malized using the absolute values for  $O^-$  [36] in the pho-  
 559 ton energy region between 2 and 3 eV where the values  
 560 of both sets of cross sections are relatively constant. The  
 561  $O^-$  cross sections were recently found to have been un-  
 562 derestimated by about 20% and to be in fact slightly in-  
 563 creasing with photon energy [3]. Renormalizing the data  
 564 from [4] using the revised photodetachment cross section  
 565 of  $O^-$  brings them into better agreement with our cur-  
 566 rent results, except for the first two values at about 1.5 eV  
 567 which are then too large.

568 The steep rise of the photodetachment cross section  
 569 above the  $C(^5S^o)$  threshold contrasts with the nearly  
 570 constant behaviour observed in this region by Haeffler  
 571 *et al.* [31]. Their results were also normalized to the  
 572 earlier photodetachment cross sections of  $O^-$  [36], but  
 573 renormalization with the absolute values by Génévriez *et al.*  
 574 [3] is inconclusive as the energy dependence is very  
 575 different and the values are very dispersed.

We also note the very good agreement between our measurements using a continuous laser and using a pulsed laser taking into account the saturation effect, validating the developments leading to the correction coefficients of Fig. 2.

In Fig. 4, the current absolute cross sections for photodetachment of  $C^-(^4S^o)$  are compared with the results of our  $R$ -matrix calculation and those by Zhou *et al.* [7]. Other theoretical studies undertaken before 2004 [37–39] have been thoroughly discussed in [2, 7], and since the agreement with experiment tends to be less good, they are not reproduced here.

Both calculations are completely *ab initio*, all coupled angular momenta are included and no energy shift was introduced. The radius  $a$  of the inner region is defined by the most diffuse atomic orbital, but as mentioned earlier, we have verified the stability of our results by performing calculations with different values of  $a$  from  $25a_0$  to  $35a_0$ , varying the number of continuum orbitals between 25 and 50, obtaining electron affinities between 1.2575 eV and 1.2613 eV. The cross sections resulting from these parametric tests are summarized in Fig. 4 by the thickness of the lines corresponding to the current  $R$ -matrix calculations. More precisely, two curves following the largest and smallest values of the calculated cross sections are plotted, and the area between them is shaded. The differences between the cross sections obtained using the length and velocity representations of the dipole matrix are very small, less than 2% over the energy range considered, which is generally a good, but not sufficient, indication of the accuracy of a calculation.

The agreement between calculation and experiment is excellent over the whole range of energy covered by the experiment. The overall agreement with the results by Zhou *et al.* [7] is also very good. The main difference is in the region just above the first photodetachment threshold where our values for the total cross section, experimental and theoretical, increase monotonically, without the narrow peak due to a slightly larger contribution from the  $C(1s^22s^22p^2^3P) + e^-(\ell = 0)$  channel in the calculations of [7].

Since the objective of [7] was to study photodetachment from threshold up to 13 eV, only one orbital ( $3d$ ) was optimized on the polarizability of the carbon ground state, while the  $3s$  and  $3p$  orbitals correspond to spectroscopic orbitals for the  $C(1s^22s^22p3s^3P^o)$  and  $C(1s^22s^22p3p^3D)$  states. In our work, the  $n=3$  and the  $4f$  orbitals are used to improve the energy of  $C(1s^22s^22p^2^3P)$ , while the  $4s$ ,  $4p$  and  $4d$  orbitals are optimized on its polarizability. The size of our  $R$ -matrix inner region ( $a=25\text{--}35a_0$ ) is hence substantially larger than in the calculations by Zhou *et al.* ( $a=23.4a_0$ ), but our computed cross sections remain stable with varying  $a$ . As a result, our calculations yield better values for the polarizability of the carbon ground state and for the electron affinity, as well as for the  $^5S^o$  threshold. Part of the difference might also be due to the treatment of the outer region. However, in previous work on photodetachment

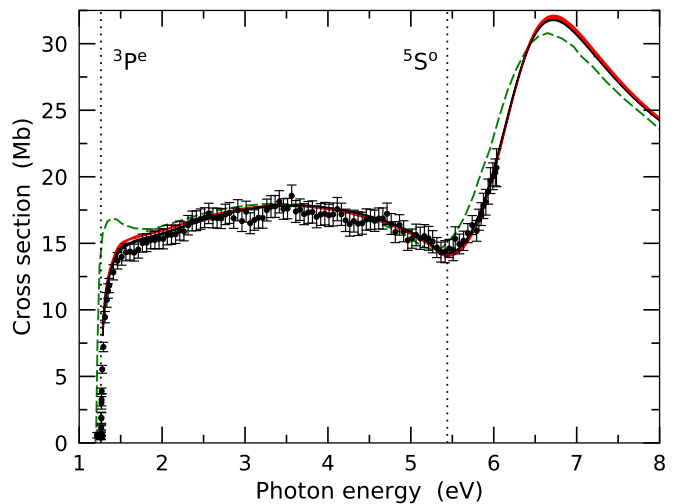


FIG. 4. Experimental and theoretical photodetachment cross sections of  $C^-(^4S^o)$  as a function of the photon energy. Full circles: present work with a pulsed laser and correction for saturation. Black full line:  $R$ -matrix method, length form; red full line:  $R$ -matrix method, velocity form; the thickness of the lines corresponds to the variation of results for different values of the calculation parameters, see text for details. Dashed line: Zhou *et al.* [7], length form. Vertical dotted lines: positions of the  $C(^3P)$  and  $C(^5S^o)$  thresholds.

of  $H^-$  [40] and  $O^-$  [11], for example, it was shown that for weak laser intensities, the perturbative approach of the UK APAP code gives results indistinguishable from those of the full  $R$ -matrix Floquet code [41, 42] that includes a numerically very robust treatment of the outer region.

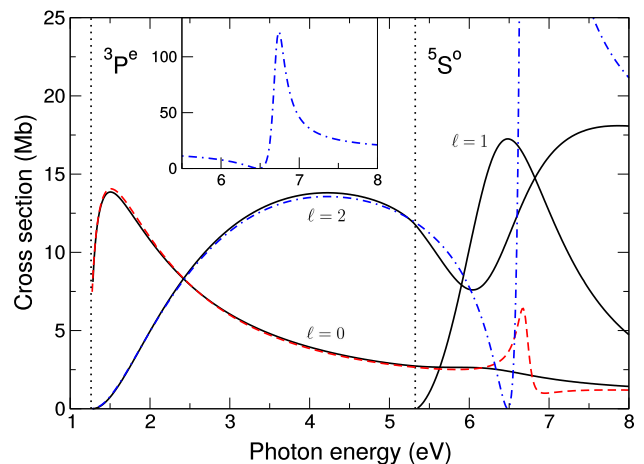


FIG. 5. Theoretical partial photodetachment cross sections as a function of the photon energy, length form. Full lines: full calculation, final channels  $C(^3P) + e^-(\ell = 0, 2)$  and  $C(^5S^o) + e^-(\ell = 1)$ ; dashed line: without  $C(^5S^o)$ , final channel  $C(^3P) + e^-(\ell = 0)$ ; dashed-dot line: without  $C(^5S^o)$ , final channel  $C(^3P) + e^-(\ell = 2)$ . Vertical dotted lines: positions of the  $C(^3P)$  and  $C(^5S^o)$  thresholds in the  $R$ -matrix calculations.

640 The total photodetachment cross section in Fig. 4 dis-  
 641 plays a broad plateau between 2.5 and 4.5 eV, then a  
 642 minimum in the vicinity of the  ${}^5S^o$  threshold followed  
 643 by a broad maximum. The plateau is the result of a  
 644 close balance between the  $\ell = 0, 2$  partial wave contribu-  
 645 tions, which are shown in Fig. 5. The structure above the  
 646  ${}^5S^o$  threshold is often referred to in the literature as a  
 647  $1s^22s2p^4{}^4P$  shape resonance (see for example [7, 39, 43–  
 648 45]). The dichotomic classification into shape resonances  
 649 (open channel resonances occurring above a threshold)  
 650 and Feshbach resonances (closed-channel resonances occur-  
 651 ing below a threshold) is however not appropriate if  
 652 electron correlations are strong and one-electron poten-  
 653 tial interaction models break down [43]. As shown in  
 654 Fig. 5, the peak above the  $C({}^5S^o)$  threshold is in fact  
 655 present even if this state is not included at all in the cal-  
 656 culation. Fig. 6 gives a schematic depiction of the differ-  
 657 ent photodetachment pathways: direct photodetachment  
 658 or excitation into a multiply excited  $C^-({}^4P)$  state em-  
 659 bedded in the continuum, followed by autodetachment.  
 660 The resonant state is represented by a shaded rectangular  
 661 area centered on the resonance position, whose vertical  
 662 extent indicates its width. When the  $C({}^5S^o)$  state is not  
 663 included in the  $R$ -matrix basis expansion, the resonance  
 664 is found at a higher energy with a greatly reduced width;  
 665 including it shifts down and broadens the resonance. The  
 666 strong interaction in the  ${}^4P$  configuration space is thus  
 667 responsible for the very broad resonance profile in the total  
 668 cross section. This is reflected in the eigenvectors of the  
 669 hamiltonian of the  $R$ -matrix inner region: in the ab-  
 670 sence of the  $C({}^5S^o)$  state, there is an eigenvalue very close  
 671 to the position of the resonance, characterized by weights  
 672 of 46%, 14% and 17% for the  $1s^22s2p^4$ ,  $1s^22s2p^3({}^5S^o)3p$   
 673 and  $1s^22s2p^3({}^5S^o)4p$  bound configurations respectively;  
 674 the remaining 23% is distributed into more excited con-  
 675 figurations. When the  $C({}^5S^o)$  state is included in the  
 676 calculation, the eigenvector of the  $R$ -matrix inner re-  
 677 gion hamiltonian associated with the resonance has a  
 678 weight of only 18% in the  $1s^22s2p^4$  configuration, 16% in  
 679  $1s^22s2p^3({}^5S^o)4p$  and 7% in  $1s^22s2p^3({}^5S^o)3p$ . The other  
 680 components are mainly those formed by  $C({}^5S^o)$  coupled  
 681 to an  $R$ -matrix continuum  $p$  orbital.

682 An efficient way of analyzing resonances is to use  
 683 the time-delay or lifetime matrix of the corresponding  
 684 electron-carbon scattering problem: even broad reso-  
 685 nances relatively close to threshold with a strong energy-  
 686 dependent background and overlapping resonances can  
 687 be fitted to Lorentzian functions whose position and  
 688 height correspond respectively to the energy and lifetime  
 689 of the resonances [46, 47]. When the  ${}^5S^o$  threshold is  
 690 omitted from the calculation, the resonance occurs at  
 691  $E_{\text{res}} = 5.457$  eV above the  $C({}^3P)$  threshold, with a width  
 692  $\Gamma = 0.177$  eV. In our full calculations, the resonance po-  
 693 sition is  $E_{\text{res}} = 4.99$  eV above the  $C({}^3P)$  threshold, corre-  
 694 sponding to a photon energy of 6.25 eV, with a width of  
 695  $\Gamma = 1.56$  eV. Furthermore, the probability of decay into  
 696 a particular open channel (autodetachment, see Fig. 6)  
 697 is given by the square of the modulus of the correspond-

698 ing element in the eigenvector associated with the largest  
 699 eigenvalue of the lifetime matrix. Using this, we find that  
 700 the probability of the resonance to decay into the  $C({}^3P)$   
 701 +  $e^-$  ( $\ell = 0$ ) channel is negligible, while the probability  
 702 of decaying into the  $C({}^3P) + e^-$  ( $\ell = 2$ ) or  $C({}^5S^o) +$   
 703  $e^-$  ( $\ell = 1$ ) channels are 0.16 and 0.84 respectively.

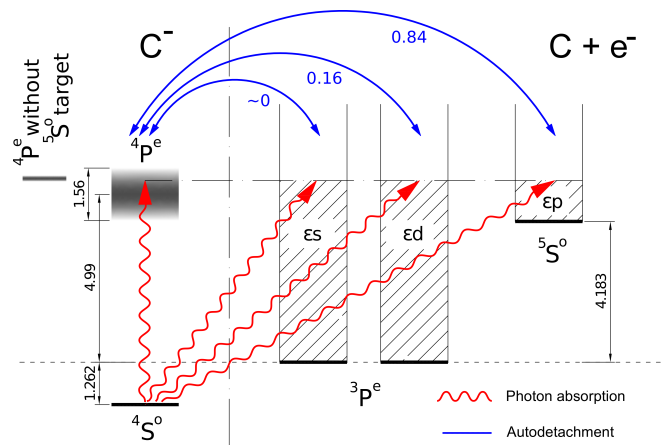


FIG. 6. Schematic representation of the photodetachment process involving an excited state of  $C^-$  embedded in three continua leading to the structure around 5.5 eV in the total cross section. The strong interaction between the  $C^-({}^4P)$  and  $C({}^5S^o)$  excited states greatly broadens and pushes down the  $C^-({}^4P)$  level, smoothing the resonance profile in the total cross section. The energy differences indicated are in eV. The shaded areas represent the positions and widths of the  ${}^4P$  resonance in the calculations with and without the  $C({}^5S^o)$  state. The numbers below the arrows indicating the different autodetachment channels are the corresponding branching ratios.

## B. Asymmetry parameter

704  
 705 In Fig. 7, we present the values of the asymmetry pa-  
 706 rameter  $\beta$  from our experiment and our  $R$ -matrix calcu-  
 707 lations, and compare them with those from earlier work  
 708 [7, 32, 33, 48].

709 Close to threshold, the dominant detachment chan-  
 710 nel corresponds to a photoelectron in the spherically  
 711 isotropic  $\ell = 0$  wave, so that  $\beta \approx 0$ . It decreases to nearly  
 712 the smallest possible value,  $-1$ , at about 2 eV before in-  
 713 creasing again to  $\beta \approx 0$ . This general trend is similar  
 714 to that for the photodetachment of  $O^-$  and reflects the  
 715 interference between the  $\ell = 0$  and  $\ell = 2$  outgoing waves.  
 716 The agreement with the few existing experimental data  
 717 by Hall *et al.* [32], Calabrese *et al.* [48] and Brandon *et al.*  
 718 [33] is very good. The agreement with the  $R$ -matrix cal-  
 719 culations is also excellent over the whole range of photon  
 720 energies considered. The small difference in the region  
 721 of the minimum at 2 eV with the calculation by Zhou *et al.*  
 722 [7] reflects the differences at low energies in the  $\ell = 0$   
 723 and  $\ell = 2$  partial cross sections shown in Fig. 5. Above  
 724 the  $C(1s^22s2p^3{}^5S^o)$  threshold, the  $\ell = 1$  channel gives

725 a constant contribution of  $\beta = 2$ , and is therefore not  
 726 shown in Fig. 7. As in the calculations by Zhou *et al.*  
 727 [7], the asymmetry parameter displays a dip above the  
 728  ${}^5S^o$  threshold; in our work, this dip is slightly deeper and  
 729 occurs at a slightly higher energy than in [7].

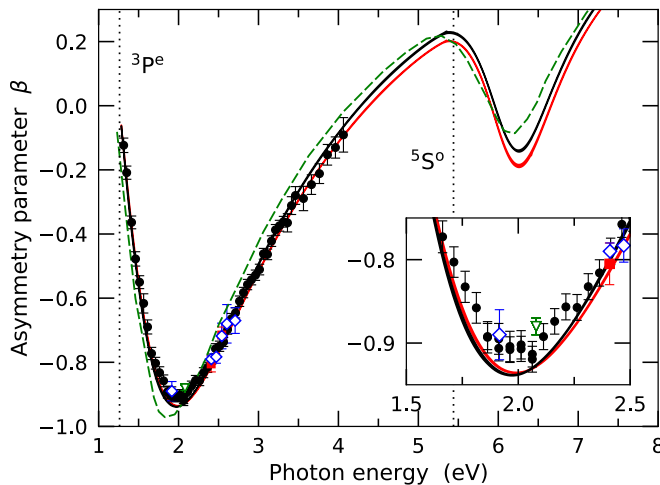


FIG. 7. Asymmetry parameter  $\beta$  for the photodetachment of  $C(4S^o)$ . Experiment: circles, present measurements; full square, Hall *et al.* [32]; open lozenge, Calabrese *et al.* [48]; open triangle down, Brandon *et al.* [33]. Theory: black full line: current  $R$ -matrix results, length form; red full line: current  $R$ -matrix results, velocity form; the thickness of the lines corresponds to the variation of results for different values of the calculation parameters, see text for details; dashed line: Zhou *et al.* [7], length form. Vertical dotted lines: positions of the  $C(3P)$  and  $C(5S^o)$  thresholds.

## V. CONCLUSION

730  
 731 Using the Animated Crossed Beam technique, we have  
 732 measured absolute cross sections for the photodetach-  
 733 ment of the ground state of carbon anion in the ground  
 734 state,  $C^-(4S^o)$ , for photon energies ranging from thresh-  
 735 old up to 6 eV. As the peak intensity of the laser is high  
 736 enough to provoke saturation in neutral production, a  
 737 correction factor has been estimated at the cost of intro-  
 738 ducing further assumptions about the laser beam profile.  
 739 We have verified that the corrected cross sections are in  
 740 excellent agreement with the uncorrected absolute cross  
 741 sections obtained using the ACB technique with contin-  
 742 uous lasers, for which saturation does not occur. We note  
 743 that the relative cross sections by Seman and Branscomb  
 744 [4], renormalized using the absolute cross sections for  $O^-$   
 745 by Génévriez *et al.* [3], tend to be in much better agree-  
 746 ment with our measurements and the best available the-  
 747 oretical predictions.

748 By analyzing the images formed by the photoelectrons  
 749 extracted from the interaction chamber through a Ve-  
 750 locity Map Imaging spectrometer, we have also deter-  
 751 mined the asymmetry parameters for photon energies

752 from threshold up to 4 eV. The results are in excellent  
 753 agreement with the few data available from previous mea-  
 754 surements [32, 33, 48].

755 The experimental study has been completed by a set  
 756 of  $R$ -matrix calculations including orbitals and pseudo-  
 757 orbitals optimized using the CIVPOL computer code to  
 758 reproduce accurate values of electron affinity and polar-  
 759 ization of the carbon ground state in an *ab initio* way.  
 760 The photodetachment cross sections in length and veloc-  
 761 ity representations are very similar, satisfying a necessary  
 762 criterion of convergence of the calculations. Our results  
 763 are in excellent agreement with the measured absolute  
 764 cross sections up to 6 eV, and are also very close to the  
 765 values determined by Zhou *et al.* [7] who used the  $R$ -  
 766 matrix method with the Variable Phase Method to treat  
 767 the outer region. Our experiment and calculations how-  
 768 ever do not reproduce the peak just above threshold ob-  
 769 tained by Zhou *et al.* The photon energy range covered  
 770 by our calculations extends up to 8 eV, which might be  
 771 somewhat high considering the absence of excited states  
 772 in our basis beyond  $C(1s^22s2p^35S^o)$ . Our results are  
 773 however in excellent agreement with the values by Zhou  
 774 *et al.* who included seven more threshold states [7] up  
 775 to nearly 11 eV, which indicates that our calculations are  
 776 converged over the whole range considered. The theoret-  
 777 ical asymmetry parameters are also in excellent agreement  
 778 with the experimental data.

779 Between the  $C(5S^o)$  threshold and 8 eV, the photode-  
 780 tachment cross section presents a broad peak which has  
 781 often been qualified as a  ${}^4P$  shape resonance with a con-  
 782 figuration  $1s^22s2p^4$  or  $1s^22s2p^3\bar{n}p$ . We have shown that  
 783 this resonance appears even in the absence of the  $C(5S^o)$   
 784 threshold, albeit with a much narrower width, provided  
 785 excitations of at least two electrons from the ground con-  
 786 figuration are taken into account. When the  $C(5S^o)$   
 787 threshold is included, continuum orbital configurations  
 788 of the form  $1s^22s2p^3(5S^o)\epsilon p$  contribute to nearly 60% of  
 789 the resonance wave function. These characteristics are a  
 790 reminder of the importance of correlation effects in open  
 791 shell systems which break the convenient system of clas-  
 792 sification of resonances based on electron in a potential  
 793 approximations.

794 A more detailed study of the photodetachment of the  
 795 excited  $C^-(2D)$  anion should also be performed in order  
 796 to verify that its contribution to the measured signal in  
 797 the current experiment is indeed negligible. It would be in-  
 798 teresting to extend the range of photon energies in order  
 799 to investigate experimentally resonances at higher ener-  
 800 gies, not just for  $C^-$  but also in heavier systems such as  
 801  $Si^-$ , but this requires the use of different light sources.

## ACKNOWLEDGMENTS

802  
 803 This work was supported by the Fonds de la Recherche  
 804 Scientifique-FNRS through IISN Contract No. 4.4504.10.  
 805 Calculations were performed on the computational clus-  
 806 ter of the Institut de Physique de Rennes.

- [1] L. M. Branscomb and B. E. J. Pagel, *Mon. Not. R. Astron. Soc.* **118**, 258 (1958).
- [2] T. Andersen, *Phys. Rep.* **394**, 157 (2004).
- [3] M. Génévriez, K. M. Dunseath, M. Terao-Dunseath, A. Hibbert, A. Dochain, R. Marion, and X. Urbain, *Phys. Rev. A* **98**, 033410 (2018).
- [4] M. L. Seman and L. M. Branscomb, *Phys. Rev.* **125**, 1602 (1962).
- [5] D. Bresteau, C. Drag, and C. Blondel, *Phys. Rev. A* **93**, 013414 (2016).
- [6] D. Feldmann, *Chem. Phys. Lett.* **47**, 338 (1977).
- [7] H. L. Zhou, S. T. Manson, A. Hibbert, L. V. Ky, N. Feautrier, and J.-C. Chang, *Phys. Rev. A* **70**, 022713 (2004).
- [8] N. D. Gibson, C. W. Walter, O. Zatsarinny, T. W. Gorczyca, G. D. Ackerman, J. D. Bozek, M. Martins, B. M. McLaughlin, and N. Berrah, *Phys. Rev. A* **67**, 030703 (2003).
- [9] A. Perry-Sassmannshausen, T. Buhr, A. Borovik, M. Martins, S. Reinwardt, S. Ricz, S. O. Stock, F. Trinter, A. Müller, S. Fritzsche, and S. Schippers, *Phys. Rev. Lett.* **124**, 083203 (2020).
- [10] P. Defrance, F. Brouillard, W. Claeys, and G. V. Wassenhove, *J. Phys. B: At. Mol. Phys.* **14**, 103 (1981).
- [11] M. Génévriez, X. Urbain, A. Dochain, A. Cyr, K. M. Dunseath, and M. Terao-Dunseath, *Phys. Rev. A* **94**, 023407 (2016).
- [12] I. León, Z. Yang, H.-T. Liu, and L.-S. Wang, *Rev. Sci. Instrum.* **85**, 083106 (2014).
- [13] C. J. Johnson, B. B. Shen, B. L. J. Poad, and R. E. Continetti, *Rev. Sci. Instrum.* **82**, 105105 (2011).
- [14] X. Urbain, D. Bech, J.-P. Van Roy, M. Géléoc, S. J. Weber, A. Huetz, and Y. J. Picard, *Rev. Sci. Instrum.* **86**, 023305 (2015).
- [15] P. Defrance, J. Lecointre, and R. Janev, in *Atomic and Plasma-Material Interaction Data for Fusion. vol. 16* (IAEA, Vienna, 2014).
- [16] A. Muller, K. Huber, K. Tinschert, R. Becker, and E. Salzborn, *Journal of Physics B: Atomic and Molecular Physics* **18**, 2993 (1985).
- [17] G. A. Alna'washi, K. K. Baral, N. B. Aryal, C. M. Thomas, and R. A. Phaneuf, *Journal of Physics B: Atomic, Molecular and Optical Physics* **47**, 105201 (2014).
- [18] P. Defrance, W. Claeys, A. Cornet, and G. Poulaert, *Journal of Physics B: Atomic and Molecular Physics* **14**, 111 (1981).
- [19] M. Génévriez, J. J. Jureta, P. Defrance, and X. Urbain, *Physical Review A* **96**, 010701 (2017).
- [20] M. Génévriez and X. Urbain, *Phys. Rev. A* **91**, 033403 (2015).
- [21] A. T. J. B. Eppink and D. H. Parker, *Rev. Sci. Instrum.* **68**, 3477 (1997).
- [22] B. Dick, *Phys. Chem. Chem. Phys.* **16**, 570 (2014).
- [23] J. C. for Guides in Metrology, *JCGM 100: Evaluation of Measurement Data - Guide to the Expression of Uncertainty in Measurement*, Tech. Rep. (JCGM, 2008).
- [24] <http://www.apap-network.org/>.
- [25] E. P. Wigner and L. Eisenbud, *Phys. Rev.* **72**, 29 (1947).
- [26] P. G. Burke, *R-matrix Theory of Atomic Collisions: Application to Atomic, Molecular and Optical Processes*, Springer Series on Atomic, Optical, and Plasma Physics, Vol. 61 (Springer, Berlin, Heidelberg, 2011).
- [27] E. Clementi and C. Roetti, *At. Data Nucl. Data Tables* **14**, 177 (1974).
- [28] V. K. Lan, M. Le Dourneuf, and P. G. Burke, *J. Phys. B: At. Mol. Phys.* **9**, 1065 (1976).
- [29] A. Kramida, Y. Ralchenko, J. Reader, and NIST ASD Team, NIST atomic spectra database (2019).
- [30] A. K. Das and A. J. Thakkar, *J. Phys. B: At. Mol. Opt. Phys.* **31**, 2215 (1998).
- [31] G. Haeffler, D. Hanstorp, I. Y. Kiyan, U. Ljungblad, H. H. Andersen, and T. Andersen, *J. Phys. B: At. Mol. Opt. Phys.* **29**, 3017 (1996).
- [32] J. L. Hall and M. W. Siegel, *J. Chem. Phys.* **48**, 943 (1968).
- [33] W. D. Brandon, D. H. Lee, D. Hanstorp, and D. J. Pegg, *J. Phys. B: At. Mol. Opt. Phys.* **31**, 751 (1998).
- [34] H.-L. Zhou, S. T. Manson, A. Hibbert, L. Vo Ky, and N. Feautrier, *Phys. Rev. A* **72**, 032723 (2005).
- [35] L. M. Branscomb, D. S. Burch, S. J. Smith, and S. Geltman, *Phys. Rev.* **111**, 504 (1958).
- [36] S. J. Smith and L. M. Branscomb, *Rev. Sci. Instrum.* **31**, 733 (1960).
- [37] G. F. Gribakin, A. A. Gribakina, B. V. Gul'tsev, and V. K. Ivanov, *J. Phys. B: At. Mol. Opt. Phys.* **25**, 1757 (1992).
- [38] C. A. Ramsbottom, K. L. Bell, and K. A. Berrington, *J. Phys. B: At. Mol. Phys.* **26**, 4399 (1993).
- [39] N. Miura, T. Noro, and F. Sasaki, *J. Phys. B: At. Mol. Opt. Phys.* **30**, 5419 (1997).
- [40] M. Dorr, J. Purvis, M. Terao-Dunseath, P. G. Burke, C. J. Joachain, and C. J. Noble, *J. Phys. B: At. Mol. Opt. Phys.* **28**, 4481 (1995).
- [41] P. G. Burke, P. Francken, and C. J. Joachain, *J. Phys. B: At. Mol. Opt. Phys.* **24**, 761 (1991).
- [42] M. Dorr, M. Terao-Dunseath, J. Purvis, C. J. Noble, P. G. Burke, and C. J. Joachain, *J. Phys. B: At. Mol. Opt. Phys.* **25**, 2809 (1992).
- [43] S. J. Buckman and C. W. Clark, *Rev. Mod. Phys.* **66**, 539 (1994).
- [44] G. Y. Kashenock and V. K. Ivanov, *Phys. Lett. A* **245**, 110 (1998).
- [45] O. Zatsarinny, K. Bartschat, L. Bandurina, and V. Gedeon, *Phys. Rev. A* **71**, 042702 (2005).
- [46] F. T. Smith, *Phys. Rev.* **118**, 349 (1960).
- [47] K. M. Dunseath, M. Terao-Dunseath, and J.-M. Launay, *J. Phys. B: At. Mol. Opt. Phys.* **33**, 3037 (2000).
- [48] D. Calabrese, A. M. Covington, D. L. Carpenter, J. S. Thompson, T. J. Kvale, and R. Collier, *J. Phys. B: At. Mol. Opt. Phys.* **30**, 4791 (1997).